Substrate Facet Effect on the Growth of Monolayer MoS_2 on Au Foils

Jianping Shi,[†,‡] Xiaona Zhang,[§] Donglin Ma,[‡] Jianbao Zhu,[⊥,∥,¶] Yu Zhang,[†,‡] Zhenxi Guo,[§] Yu Yao,[⊥,∥] Qingqing Ji,[‡] Xiuju Song,[‡] Yanshuo Zhang,[†,‡] Cong Li,[†,‡] Zhongfan Liu,[‡] Wenguang Zhu,[*,⊥,∥,¥] and Yanfeng Zhang[*,†,‡]

[†]Department of Materials Science and Engineering, College of Engineering, Peking University, Beijing 100871, People's Republic of China, [‡]Center for Nanochemistry (CNC), Beijing Science and Engineering Center for Nanocarbons, Beijing National Laboratory for Molecular Sciences, College of Chemistry and Molecular Engineering, Peking University, Beijing 100871, People's Republic of China, [§]Institute of Microstructure and Property of Advanced Materials, Beijing University of Technology, Beijing 100124, People's Republic of China, [⊥]International Center for Quantum Design of Functional Materials (ICQD), Hefei National Laboratory for Physical Sciences at the Microscale (HFNL), University of Science and Technology of China, Hefei, Anhui 230026, People's Republic of China, [∥]Key Laboratory of Strongly-Coupled Quantum Matter Physics, Chinese Academy of Sciences, School of Physical Sciences, University of Science and Technology of China, Hefei, Anhui 230026, People's Republic of China, [¥]Synergetic Innovation Center of Quantum Information and Quantum Physics, University of Science and Technology of China, Hefei, Anhui 230026, People's Republic of China, and [¶]Beijing Computational Science Research Center, Beijing, 100084, People's Republic of China

ABSTRACT MoS_2 on polycrystalline metal substrates emerges as an intriguing growth system compared to that on insulating substrates due to its direct application as an electrocatalyst in hydrogen evolution. However, the growth is still indistinct with regard to the effects of the inevitably evolved facets. Herein, we demonstrate for the first time that the crystallography of Au foil substrates can mediate a strong effect on the growth of monolayer MoS_2, where large-domain single-crystal MoS_2 triangles are more preferentially evolved on Au(100) and Au(110) facets than on Au(111) at relative high growth temperatures (>680 °C). Intriguingly, this substrate effect can be weakened at a low growth temperature (∼530 °C), reflected with uniform distributions of domain size and nucleation density among the different facets. The preferential nucleation and growth on some specific Au facets are explained from the facet-dependent binding energy of MoS_2 according to density functional theory calculations. In brief, this work should shed light on the effect of substrate crystallography on the synthesis of monolayer MoS_2, thus paving the way for achieving batch-produced, large-domain or domain size-tunable growth through an appropriate selection of the growth substrate.

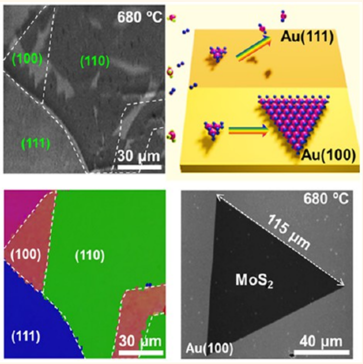

KEYWORDS: molybdenum disulfide · substrate crystallography · chemical vapor deposition · electron backscatter diffraction

In recent years, the startling discovery of graphene[1] and the subsequent detection of some intriguing physical issues like the quantum Hall effect[2] have ignited global interest in constructing a variety of other two-dimensional (2D) layered materials. Among them, transition metal dichalcogenides (TMDCs), such as monolayer MX_2 (M = Mo, W and X = S, Se), have recently attracted enormous attention.[3] These single layers consist of two close-packed chalcogenide planes sandwiching a transition metal layer in a trigonal prismatic X−M−X configuration. This unique structure endows MX_2 with exceptional physical properties and a wide range of potential applications.[4,5] Molybdenum disulfide (MoS_2), a widely studied semiconducting TMDC, possesses an indirect band gap of 1.3 eV in bulk and a direct band gap of 1.9 eV in the monolayer.[6] This indirect to direct band gap transition not only leads to fascinating valley-related physics but also opens up novel applications, such as optoelectronics,[7−9] valleytronics,[10−12] light absorption,[13,14] and hydrogen evolution reaction (HER).[15−17]

However, controllable synthesis of large-domain monolayer MoS_2 is a prerequisite for fulfilling these application potentials. For the time being, a variety of methods, such as micromechanical exfoliation and decomposition of thiomolybdates, have been reported to obtain high-quality MoS_2.[18,19] However, these methods seem to be either not compatible with large-scale production or not easy for a strict control of the layer thickness. Compared with the above-mentioned routes, the chemical vapor deposition (CVD) technique has shown promise for generating high-quality MoS_2 layers with scalable size, controllable thickness, and high crystal quality.[20−25] The obtained

* Address correspondence to
yanfengzhang@pku.edu.cn,
wgzhu@ustc.edu.cn.

Received for review January 6, 2015
and accepted March 23, 2015.

10.1021/acsnano.5b00081

MoS_2 monolayers can be used as active components for nanoelectronics as well as building blocks for constructing layered heterostructures.[26] However, it is worthy of mentioning that MoS_2 films are generally obtained on insulating substrates,[27−30] and only a few groups have worked on the synthesis of MoS_2 on conducting substrates (such as Au foils and graphene).[17,19] This new growth system is highly desired considering that directly grown MoS_2 on metal substrates should be compatible with direct atomic-scale characterizations using scanning tunneling microscopy and spectroscopy (STM/STS), thus revealing some fundamental properties of the monolayer material. The direct application in HER is also an interesting topic due to the exclusion of a tedious sample transfer process and the probable quality degradation.[15,17,31]

Although the metal substrate is likely to be the optimum choice for obtaining large-domain and strictly monolayer MoS_2,[17,24,31] different facets usually evolve after the CVD growth process. It is worth reminding that, according to both experimental results and theoretical calculations,[32−34] the different facets of polycrystalline Cu foils and other metal foil substrates have been reported to imply a tremendous effect on the growth of graphene mainly on the domain shape/orientation, stacking geometry, and growth rate/thickness. Hereby, it is crucial to intensively explore the effect of different facets of metal foils on the growth of MoS_2 for the purpose of further increasing the domain size and the crystal quality as well as for a deeper understanding of the growth mechanism.

In this work, we have selected polycrystalline Au foils as the substrates for CVD synthesis of MoS_2, due to its chemical inertness for S vapor. We wish to address the effect of the inevitably evolved facets on the growth of MoS_2. Intriguingly, we find that large-domain monolayer MoS_2 triangles preferentially nucleate and grow on Au(100) and Au(110) facets rather than on Au(111) at relatively high growth temperatures (>680 °C). However, the modulation effect of Au facets on MoS_2 growth seems to be greatly weakened at a relative low growth temperature (∼530 °C), with the formation of uniformly distributed MoS_2 flakes showing nearly uniform domain sizes. Briefly, this discovery is expected to shed light on the selection of appropriate metal substrates for MoS_2 synthesis toward achieving batch-produced, large-domain, and high-quality materials.

RESULTS AND DISCUSSION

Triangular MoS_2 flakes were synthesized directly on Au foils in a low-pressure CVD (LPCVD) system with the method described elsewhere.[17,20−27] In order to remove impurities and reconstruct the single-crystalline surface, first, the Au foil substrates were annealed at 900 °C for 1 h under 50 sccm Ar and 20 sccm H_2 carrier gas conditions. X-ray diffraction (XRD) patterns were then recorded from the same sample before and after growth of MoS_2 at 530 °C to reveal the Au crystal structure (Figure 1b), which have also been compared with standard XRD for Au (JCPDS data: PDF number 00-004-0784). A crystallographically diverse Au surface, composed of Au(100), Au(110), Au(111), and Au(311) facets, was shown clearly, with the former two facets presenting a much larger ratio. The facet-dependent growth behavior of MoS_2 on Au foils is vividly shown in Figure 1a.

According to scanning electron microscopy (SEM) images in Figure 1c, triangular MoS_2 flakes with relative uniform distributions can be obtained on different grains (usually corresponding to different facets) of Au foils. More low-magnification SEM images of MoS_2 triangles on different Au grains are also presented in Supporting Information Figure S1. Here, the substrate grain boundaries are indicated by the dotted lines.

In order to visually image the crystal structure of the underlying Au foil, SEM images (Figure 1d,f) and corresponding electron backscatter diffraction (EBSD) maps (Figure 1e,g) were captured to correlate the edge length and the flake shape of MoS_2 triangles with the crystallographic orientation of Au grains. Evidently, Figure 1d shows the SEM image of MoS_2 triangles on two Au grains of Au(100) and Au(111), which are determined by the corresponding EBSD map in Figure 1e. The domain size of MoS_2 triangles on Au(100) seems a little larger than that of its neighboring Au(111) facet. However, the coverage of MoS_2 on Au(100) is a little lower than that of Au(111). In contrast, Figure 1f demonstrates the different growth result of MoS_2 triangles on another two Au facets of Au(110) and Au(111). Notably, larger-domain MoS_2 triangles evolve preferably on the Au(110) facet than on Au(111).

For more details, high-magnification SEM images of MoS_2 triangles on three representative Au facets are presented in Figure 1h. The statistical distribution of the MoS_2 domain size is displayed in Figure 1i, with the average edge length of 0.47 ± 0.03, 0.50 ± 0.05, and 0.36 ± 0.01 μm for Au(100), Au(110), and Au(111), respectively. Furthermore, Raman spectroscopy was also employed to show the thickness of MoS_2 on different Au facets. Two typical Raman peaks corresponding to the out-of-plane vibration of S atoms (A'_1) at ∼406.9 cm^{-1} and in-plane vibration of Mo and S atoms (E') at ∼387.0 cm^{-1} were obtained to be invariable with the different Au facets.[35] The frequency difference, $\Delta \sim 19.9$ cm^{-1}, acquired from different Au facets, is in good agreement with those reported for monolayer MoS_2.[36] These facts indicate the monolayer thickness of MoS_2 on Au foils regardless of the Au crystallographic orientation. The growth is thus expected to obey a surface-limited mechanism.

More low-magnification SEM images and corresponding EBSD maps of MoS_2 on different Au facets are shown in the Supporting Information Figure S2. Based on these results, it can be inferred that, at a low growth temperature of ∼530 °C, the different facets of

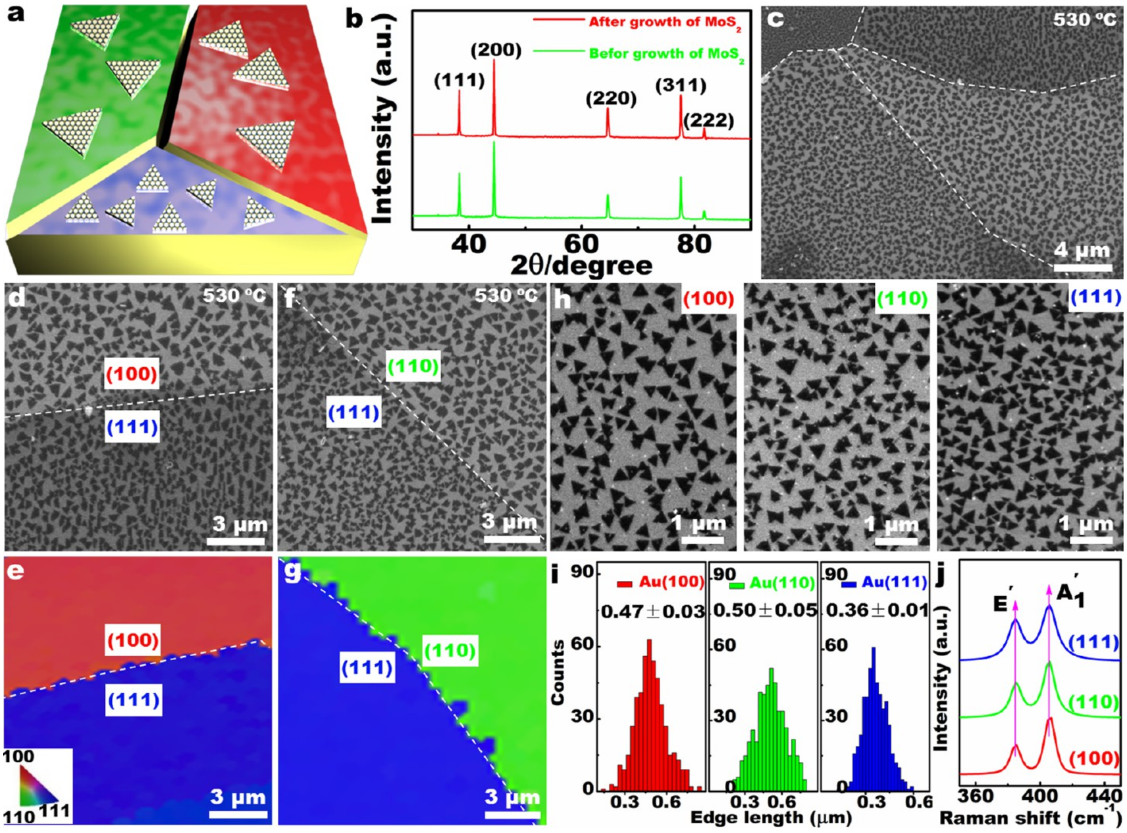

Figure 1. Edge length dependence of MoS$_2$ triangles on the facets of Au foils (synthesized at 530 °C for 1 h under 50 sccm Ar carrier gas). (a) Schematic view of MoS$_2$ growth on different Au facets. (b) XRD patterns captured from a sample before and after growth. (c) Low-magnification SEM image of MoS$_2$ synthesized on different Au facets, with the dotted lines indicating the substrate grain boundaries. (d,f) SEM images of MoS$_2$ triangles on neighboring facets of Au(100), Au(110), and Au(111). (e,g) Corresponding electron backscatter diffraction (EBSD) images of (d) and (f) using the standard EBSD color key. (h) High-magnification SEM images of triangular MoS$_2$ flakes on three representative Au facets. (i) Edge length statistics of the triangular MoS$_2$ flakes in (h) with regard to different Au facets (statistics based on SEM images including at least 300 flakes). (j) Raman spectra captured from MoS$_2$ flakes grown on the three representative Au facets.

Au foils can imply a very minor effect on the domain size/shape and coverage of MoS$_2$ under the same growth condition. The triangular edge length of monolayer MoS$_2$ is usually variable from ~0.36 to 0.50 μm.

Upon increasing the growth temperature to 610 °C, the edge length of MoS$_2$ triangles was increased accordingly along with an obvious coverage decrease, as shown in the large-scale SEM image in Figure 2a. Meanwhile, the edge length and shape of MoS$_2$ flakes present clear differences on disparate Au grains. Similarly, a corresponding EBSD image of the same region was obtained to show the underlying facets of Au(100), Au(111), and Au(311) (Figure 2b). It can be noticed that large-domain triangular and polygonal MoS$_2$ flakes with sharp edges were evolved on Au(100). In contrast, relatively small and irregular MoS$_2$ flakes with uniform size were achieved on Au(111) and Au(331) facets. Further high-magnification SEM images and corresponding EBSD maps of MoS$_2$ flakes on three representative Au facets (Au(100), Au(110), and Au(111)) are displayed in Figure 2c–f (Supporting Information Figure S3). In order to give a quantitative result, the average edge lengths of MoS$_2$ triangles on Au(100), Au(110), and Au(111) facets are statistically calculated to be 5.6 ± 1.5, 5.8 ± 1.3, and 2.8 ± 0.5 μm, respectively (Figure 2g). A clear difference for MoS$_2$ growth between the former two facets and the latter one can be clearly identified.

Raman spectroscopy and mapping methods were also applied to confirm the thickness and the uniformity of MoS$_2$ flakes on different Au facets (Figure 2h and Supporting Information Figure S4). The typical vibrations modes (A′$_1$, E′) for MoS$_2$ flakes on three representative Au facets (Au(100), Au(110), and Au(111)) (Figure 2h) exhibit almost the same locations with the same frequency difference of $\Delta \sim 19.9$ cm^{-1}. These suggest the monolayer feature of MoS$_2$ triangles on different Au facets. Besides, rather homogeneous contrasts in the Raman mapping image reconfirm the rather high thickness uniformity of MoS$_2$ flakes on different Au facets (Supporting Information Figure S4). Briefly, for MoS$_2$ grown on Au foils at 610 °C, the flake size is greatly increased due to the enhanced growth temperature, and the nucleation density is dramatically decreased. Regardless of the underlying facet alternation, the obtained layer thickness is always

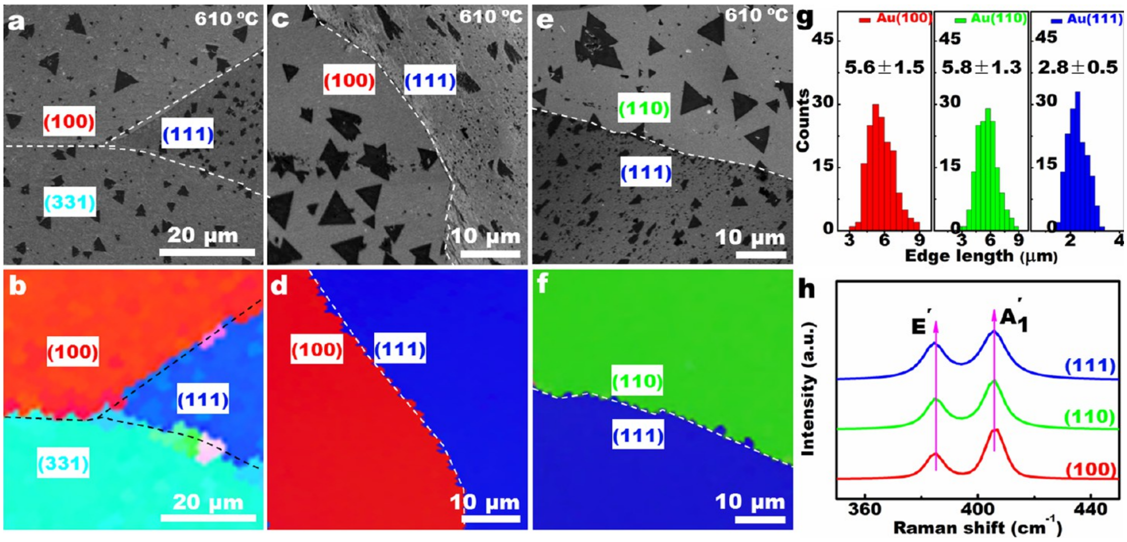

Figure 2. Edge length and shape dependence of MoS_2 flakes on the facets of Au foils at a medium growth temperature of ∼610 °C (CVD growth for 1 h under 50 sccm Ar carrier gas). (a) Low-magnification SEM image of MoS_2 flakes on three facets of Au foils (Au(100), Au(111), and Au(331)), with the dotted lines indicating the substrate grain boundaries. (b) Corresponding EBSD image of the same region in (a) using the standard EBSD color key. (c,e) High-magnification SEM images of MoS_2 on two neighboring Au facets of Au(100) and Au(111), and Au(110) and Au(111), respectively. (d,f) Corresponding EBSD images of the same regions of (c) and (e), respectively. (g) Edge length statistics of MoS_2 flakes on three representative Au facets (statistics based on SEM images including at least 100 flakes). (h) Raman spectra of the MoS_2 flakes on different Au facets.

of a monolayer. An obvious modulation effect of different Au facets on the flake size/uniformity of MoS_2 was noticed.

In order to clarify the edge length evolution of MoS_2 triangles on different Au facets, even high growth temperatures of 680 and 750 °C were selected. The schematic view in Figure 3a visually displays the different growth behavior. Uniform triangular and polygonal MoS_2 flakes were obtained on specific Au facets, while with the neighboring facets were free of MoS_2, as shown by the SEM images in Figure 3b,c. Notably, the edge lengths of the triangular MoS_2 flakes are greatly enhanced (∼50 μm at large) along with a dramatic decrease of the nucleation density. More low-magnification SEM images of large-domain MoS_2 flakes on different Au facets are shown in Supporting Information Figure S5, where nearly complete coverage of MoS_2 films is observed preferentially on special Au facets.

To determine the facet effect, SEM images of monolayer MoS_2 flakes on distinct Au facets grown at 680 and 750 °C were achieved (Figure 3d,f and h,j). Herein, large-domain and high-coverage MoS_2 films are observed on the facets of Au(100), Au(110), and Au(310). Intriguingly, no MoS_2 flakes evolve on Au(111), as determined by corresponding EBSD maps (Figure 3e, g and i,k). Raman mapping images in Supporting Information Figure S6 show more evidence of the relatively high thickness uniformity and the high crystal quality of monolayer MoS_2 grown at relatively high temperatures of 680 and 750 °C.

As mentioned above, through a combination of SEM and EBSD techniques, a facet-dependent growth behavior of MoS_2 on Au foils can be definitely defined and featured with different domain size/shape and coverage. Intriguingly, the MoS_2 flakes as-grown on Au foils can be recognized by optical microscope (OM) images according to their different contrasts with regard to the growth substrate. Hereby, based on surface morphology analysis *via* optical image and/or Raman mapping data, the underlying facet components can be tentatively defined.

Figure 4a shows the OM image of monolayer MoS_2 flakes grown at 680 °C on two Au grains (marked by (1) and (2)), where the grain boundaries and MoS_2 flake edges are highlighted by the dotted lines and solid lines, respectively. It is interesting to find that MoS_2 flakes prefer to nucleate on the terrace marked by (1) (top right region) and along the Au grain boundary. However, no MoS_2 flakes can evolve on the lower left Au grain (marked by (2)). Significantly, while polycrystalline MoS_2 flakes can be noticed to grow right along the boundary of grain (1), they cannot spill over the boundary to the adjacent grain (marked by (2)). This result behaves as perfect evidence of the preferred growth on grain (1) than on grain (2). According to the aforementioned discussion, the Au grain marked by (2) can be tentatively determined as Au(111), and the other Au grain marked by (1) possibly belongs to a low-index facet of Au(100) or Au(110). Raman mapping for the same region of Figure 4a visually reveals the selective growth result of MoS_2 on distinct Au facets (Figure 4b). Furthermore, single-point Raman spectra from specific positions (Figure 4c), as indicated by the dots in Figure 4a, shows the monolayer nature of MoS_2 on the same grain (marked by (1)). The OM and Raman mapping image of MoS_2 flakes grown at 750 °C on three Au grains (marked by (1), (2), and (3)) are also

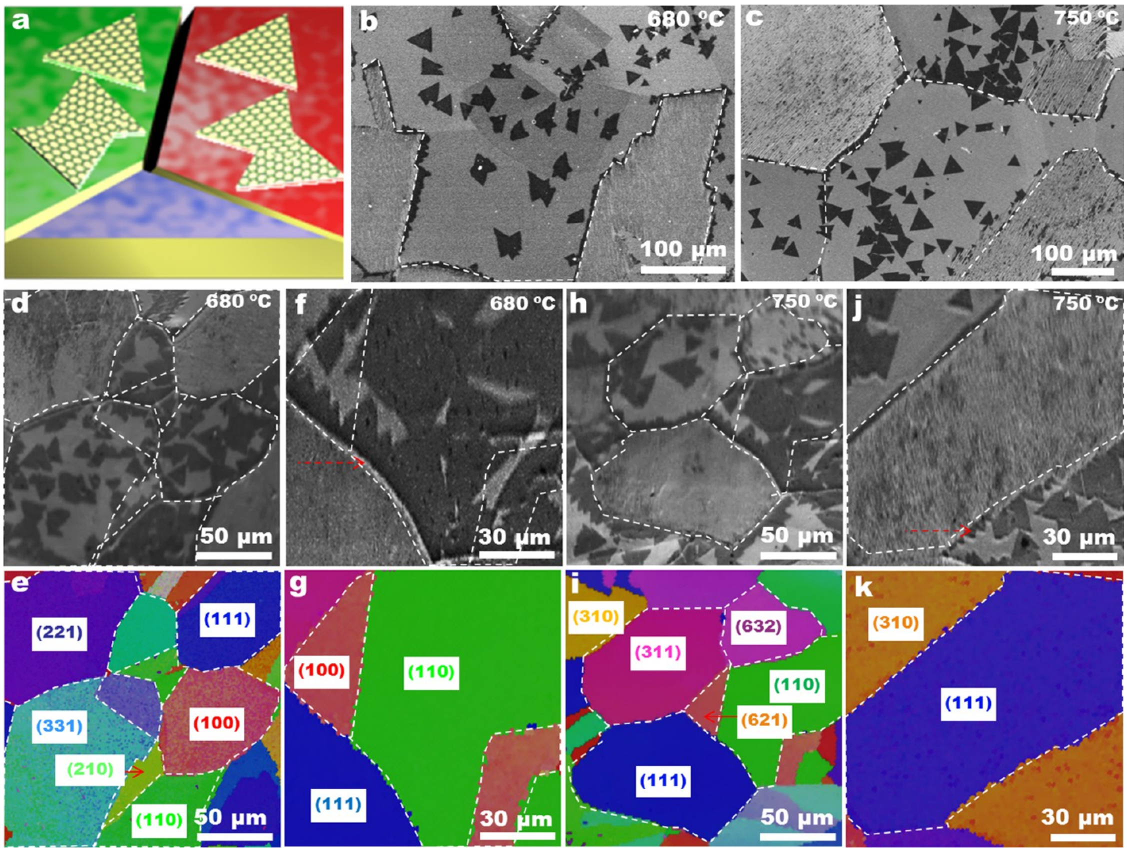

Figure 3. Edge length dependence of MoS_2 flakes on the facets of Au foils grown at relative high temperatures of 680 and 750 °C (CVD growth for 1 h under 50 sccm Ar carrier gas). (a) Schematic view presenting the morphology of MoS_2 grown on different Au facets. (b,c) Low-magnification SEM images of MoS_2 flakes on different Au facets, with the dotted lines indicating the grain boundaries of Au foils. (d,e) SEM image and EBSD map of large-domain MoS_2 triangles on distinct Au facets grown at 680 °C. (f,g) High-magnification SEM and corresponding EBSD images presenting the preferred growth of MoS_2 flakes on two Au facts of Au(100) and Au(110). (h,i) SEM image and corresponding EBSD map of MoS_2 triangles grown at 750 °C. (j,k) High-magnification SEM and EBSD images of MoS_2 flakes grown on two Au facets of Au(111) and Au(310).

displayed in Figure 4d,e. A preferred growth of MoS_2 on the top two grains can be clearly noticed by the OM image and corresponding Raman mapping data. Intriguingly, a corner of the butterfly-like MoS_2 flake can ride over the grain boundary of grain (3) and extend to grain (1). In contrast, no MoS_2 flake can be identified to grow on the other grain (2). Hereby, the Au grain marked by (2) can be tentatively determined as Au(111); the other two Au grains should correspond to low-index Au facets. Notably, when the MoS_2 flake spills over the boundary of grain (1) and grain (3), its sharpness and orientation are nearly unchanged, as indicated by the red arrow in Figure 4d,e. This indicates the similar growth mechanism of MoS_2 on these two Au grains. Raman spectra from specific positions (as indicated by the dots in Figure 4d) reconfirm the selective growth result of MoS_2 on different Au facets, according to the occurrence of a typical Raman signal of MoS_2 (Figure 4f).

A wet chemical etching method was then applied to transfer the as-grown samples onto other substrates. According to OM images shown in Figure 4g, a perfect preservation of the flake shapes can be obtained after sample transference onto a quartz substrate. By virtue of atomic force microscopy (AFM) and transmission electron microscopic (TEM) analysis (Figure 4h,i), the thickness of MoS_2 flakes derived from various facets of Au can be strictly determined to be monolayer (Figure 4f). The relative high crystal quality of the transferred sample can be confirmed from the perfect atomic lattice of MoS_2 (in the inset of Figure 4i). Moreover, a number of wrinkles, usually possessing a height of >1 nm, are generated from the transfer process.

The above experimental results clearly indicate that, at relatively high temperatures (>610 °C), MoS_2 triangles are more preferentially evolved on Au(100) and Au(110) facets than on Au(111). Interestingly, a similar observation has been reported in the growth of graphene on Cu foils.[34] The stronger binding of carbon species on Cu(100) compared to that on Cu(111), obtained from first-principles calculations and rate equation analysis, is considered the probable reason.

The growth process of MoS_2 on Au(100) and Au(111) facets should be much more complicated than that of graphene, as schematically illustrated in Figure 5a. The upstream MoO_3 precursor was partially reduced by

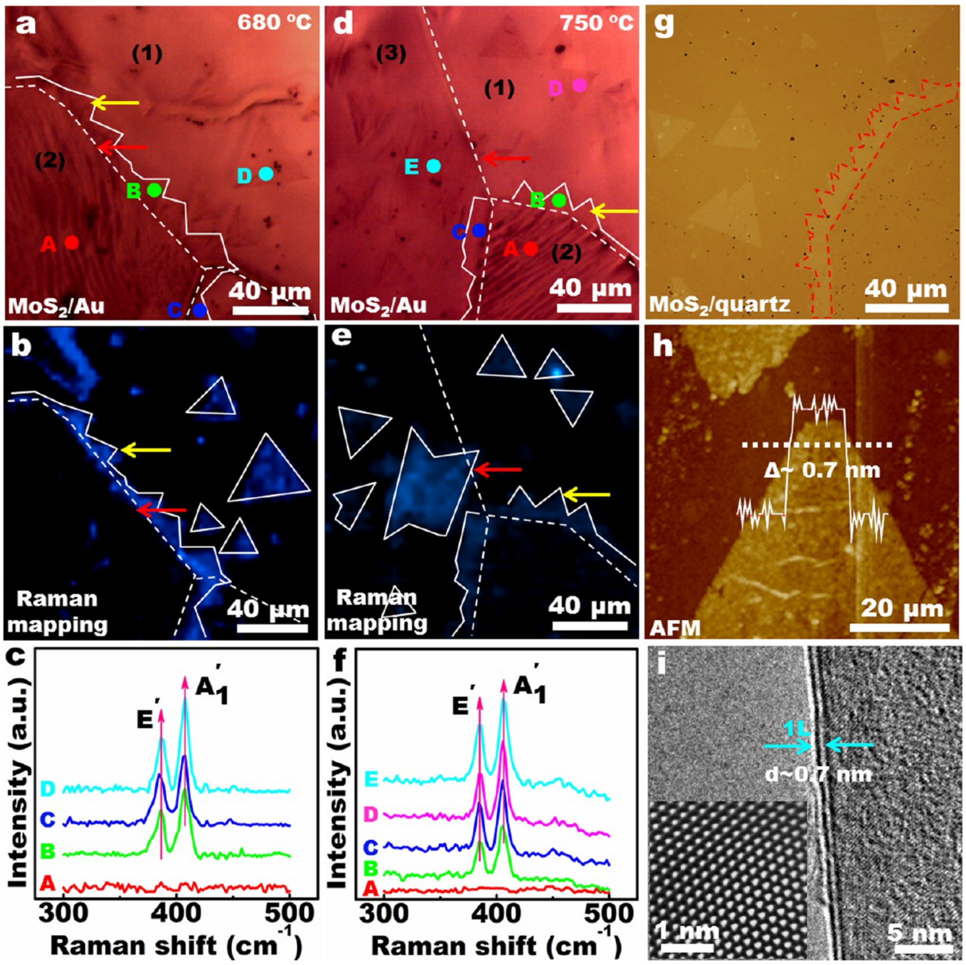

Figure 4. OM, Raman, AFM, and TEM characterizations of MoS_2 as-grown on polycrystalline Au foils and after being transferred onto quartz and SiO_2/Si substrates. (a) OM image of large-domain MoS_2 flakes grown at 680 °C, with the dotted lines and solid lines showing the boundaries of Au grains and the edge of MoS_2 flakes, respectively. (b) Corresponding Raman mapping image of the same region with the solid lines showing the edge of MoS_2 flakes. (c) Raman spectra captured from the marked spots in (a). (d,e) OM and Raman mapping images of MoS_2 triangles on different Au facets grown at 750 °C. (f) Raman spectra obtained from the marked spots in (d). (g) OM image of monolayer MoS_2 flakes after being transferred onto quartz substrates with the white lines showing the edge of MoS_2 flakes. (h) AFM image of a MoS_2 triangle after being transferred onto SiO_2/Si and corresponding section view along the dashed line showing the monolayer feature (~0.7 nm in apparent height). (i) TEM image on a folded edge indicating the monolayer nature of the MoS_2 flake. The inset is the atomic resolution image of MoS_2.

vaporized S to form volatile suboxide species of MoO_{3-x} and then sulfurized into MoS_2 on the downstream substrate with the aid of Ar carrier gas. To elucidate the underlying mechanism of the observed facet-dependent growth of MoS_2 in the current experiments, the binding energies of the precursors (single S atoms, S_2 molecules, and MoO_3) and several possible reactants (MoS, MoS_2, and MoS_3) on Au(111) and Au(100) were calculated by using first-principles calculations within density functional theory (DFT). The most stable adsorption geometries of several possible reactants on Au(100) and Au(111) and are shown in Figure 5b, and the related data for precursors are listed in the Supporting Information Figure S7. It is obvious to see that the binding energies of the precursors on Au(111) and Au(100) are very close to each other, but the binding of the reactants is consistently stronger on Au(100) than on Au(111) ($E_b^{(100)}$ = 4.87, 4.67, 4.87 eV; $E_b^{(111)}$ = 4.09, 4.37, 4.28 eV, respectively). The binding energy difference may explain the observed preferential growth of MoS_2 on the Au(100) facets at high temperatures (>610 °C), analogous to the case of the graphene growth on Cu foils.

From the evolution of the MoS_2 coverage as a function of temperature, it is clear to find that, on the Au(100) facet, the coverage of MoS_2 continuously increases until 680 °C and then decreases slightly at 750 °C for the same growth time (~10 min). However, on the Au(111) facet, the coverage suddenly drops to almost zero from 610 to 680 °C. To explain this intriguing issue, note that, at low growth temperature of ~530 °C, the Au(111) herringbone reconstruction may occur,[37−39] which is probably active for adsorbing MoS_x and for the subsequent growth of MoS_2. At high temperatures (>610 °C), due to the phase transition from the herringbone reconstruction to the

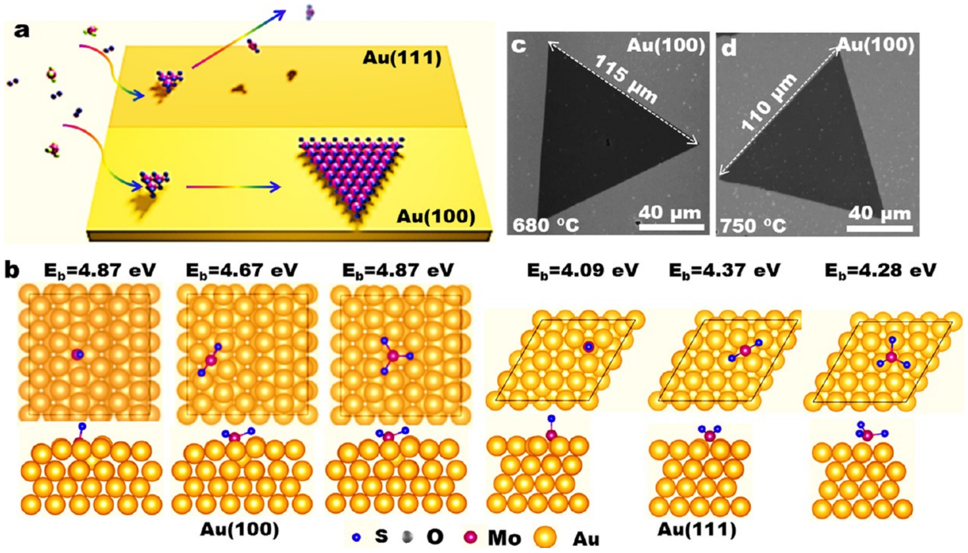

Figure 5. Theoretical calculations of the binding energies of MoS_x ($x = 1-3$) on Au(100) and Au(111) facets and experimental data of large-domain growth of monolayer MoS_2 on the Au(100) facet. (a) Schematic view of the surface growth of MoS_2 on Au(100) and Au(111) facets. (b) Top and side views of the most stable adsorption geometries of MoS_x on (5 × 1) reconstructed Au(100) and on Au(111) facets. (c,d) SEM images of large-domain monolayer MoS_2 triangles grown on Au(100) facets at 680 and 750 °C, respectively.

unreconstructed, the nucleation and growth of MoS_2 on the Au(111) facet should be dramatically decreased. That means the phase transition induced by temperature increase may contribute another possible reason for MoS_2 growth from homogeneous to inhomogeneous on the different Au facets. However, it is noteworthy that a complete understanding of the chemical reactions involved in the MoS_2 growth process is still challenging from theoretical calculations. A thorough investigation of the atomistic mechanism for MoS_2 CVD growth on Au substrates would be a subject of future studies.

Considering that monolayer MoS_2 triangles are more preferentially evolved on Au(100) and Au(110) facets than on Au(111), the selection of the former two facets is hereby crucial for achieving large-scale uniform or large-domain monolayer MoS_2. Annealing Au foils under high Ar/H_2 ratio[40] or high vacuum deposition Au films on a Si single crystal[41] may be helpful for the production of Au(100) and Au(110) facets. Notably, on the Au(100) facet of Au foils, large-domain monolayer MoS_2 triangles with an edge length of ~115 μm can be achieved by introducing H_2 as the carrier gas (Figure 5c,d).

CONCLUSION

We have demonstrated a facet-dependent growth behavior of monolayer MoS_2 on Au foils. Au(100) and Au(110) facets are found to be preferable for growing large-domain monolayer MoS_2 at relatively high temperatures (>680 °C). However, a uniform growth of small-domain MoS_2 occurs at a relatively low temperature of 530 °C, regardless of the different facets of Au foils. This interesting growth result is explained tentatively from the different binding energies of MoS_2-related species on different Au facets. This work not only presents the effect of substrate crystallography on the synthesis of monolayer MoS_2 but also proposes a probability of synthesizing large-domain and high-quality monolayer MoS_2 through the viewpoint of designing a suitable growth substrate.

METHODS

Growth of Monolayer MoS_2 on Au Foils and Transfer onto Other Substrates. A LPCVD system was applied for growth of monolayer MoS_2 on Au foils. This system was composed by a multi-temperature-zone tubular furnace (Lindberg/Blue M) equipped with a 1 in. diameter quartz tube. Sulfur powders (Alfa Aesar, purity 99.5%), placed outside the hot zone, were mildly sublimated at ~102 °C with heating belts and carried by Ar gas (50 sccm) to the downstream growth zone. MoO_3 powders (Alfa Aesar, purity 99.9%) and Au foils (Alfa Aesar, purity 99.985%, thickness ~25 μm) were successively placed on the downstream region of the quartz tube. By placing a heat insulator between MoO_3 powders and Au foils, the vaporization temperature (of MoO_3) and the deposition temperature (of MoS_2) can be controlled, separately. The MoO_3 powders were heated from room temperature to ~530 °C within 30 min along with a heating rate of ~17 °C/min, and the Au foil substrate was heated to ~530, 610, 680, and 750 °C within 30 min. The growth time was set at 60 min for all of the samples. To transfer MoS_2 films onto other substrates, the MoS_2/Au sample was first coated with poly(methyl methacrylate) (PMMA) by spin-coating at 3000 rpm for 60 s and then baked at 170 °C for 10 min. Second, the PMMA-coated sample was then etched in Au etchant (KI/I_2, a mixing ratio of $KI/I_2/H_2O$ = 4 g/1 g/40 mL) to remove the backside Au. Finally, the PMMA-supported MoS_2 was fished out by a fresh SiO_2/Si (or other substrates) followed by annealing on a hot plate at 150 °C for 10 min to remove water and immersing in an acetone bath for 5 min to remove the capping PMMA.

Characterizations of Monolayer MoS_2. The prepared MoS_2 flakes were systematically characterized through optical microscopy (Olympus DX51), Raman spectroscopy (Horiba, LabRAM HR-800, excitation light ~514 nm), and SEM (Hitachi S-4800, acceleration voltage of 1−5 kV), and EBSD was collected using a JEOLJSM-6500F analytical SEM with Oxford Technology EBSD System. During EBSD collection, the probe current was 5 nA, the accelerating voltage was 20 kV, and the angle of incidence was 70°. AFM utilized a Vecco Nanoscope III, and HRTEM used a JEOLJEM-2100F LaB6 (acceleration voltage, 200 kV).

DFT Calculations. The DFT calculations were carried out using the Vienna ab initio simulation package (VASP) with projector-augmented wave (PAW) pseudopotentials and the generalized gradient approximation in the parametrization of Perdew, Burke, and Enzerhof for the exchange-correlation functional.[42−45] The plane wave expansions were determined by the default energy cutoffs given by the VASP PAW potentials. The optimized lattice constant of Au is 4.174 Å, in good agreement with the experimental value of 4.078 Å. The Au(111) facet was modeled by an unreconstructed 4 × 4 surface slab, and the Au(100) facet was modeled by a 5 × 5 surface slab with the top layer of Au atoms reconstructed into a quasihexagonal close-packed structure.[46] Both slabs contain four atomic layers with a vacuum region of ~20 Å. During structural relaxation, the bottom two layers were fixed at their bulk positions, with all the other atoms fully relaxed until the force on these atoms were all smaller than 0.01 eV/Å. A 5 × 5 × 1 and a 3 × 3 × 1 *k*-point mesh were used to sample the Brillouin zone of the supercells. The Fermi level smearing approach of Methfessel and Paxton was employed at a width of 0.1 eV.[47] The van der Waals interactions between the adsorbates and the substrates were included using the semiempirical DFT-D_3 method with Becke−Jonson damping.[48,49]

Conflict of Interest: The authors declare no competing financial interest.

Acknowledgment. This work was financially supported by National Natural Science Foundation of China (Grant Nos. 51222201, 51290272, 21201012, 51121091, 51472008, 51072004, and 51201069) and the Ministry of Science and Technology of China (Grant Nos. 2011CB921903, 2012CB921404, 2012CB933404, 2013CB932603, and 2011CB933003). Work by J.Z., Y.Y., and W.Z. was supported by the National Natural Science Foundation of China (Grant Nos. 11374273 and 11034006) and the Fundamental Research Funds for the Central Universities (Grant Nos. WK2090050027, WK2060190027, WK2340000063).

Supporting Information Available: More Raman spectra, OM, SEM, EBSD, and Raman mapping data of as-grown MoS_2 on Au foils. This material is available free of charge *via* the Internet at http://pubs.acs.org.

REFERENCES AND NOTES

1. Geim, A. K.; Novoselov, K. S. The Rise of Graphene. *Nat. Mater.* **2007**, *6*, 183–191.
2. Novoselov, K. S.; Jiang, Z.; Zhang, Y.; Morozov, S.; Stormer, H.; Zeitler, U.; Maan, J.; Boebinger, G.; Kim, P.; Geim, A. K. Room-Temperature Quantum Hall Effect in Graphene. *Science* **2007**, *315*, 1379–1379.
3. Wang, Q. H.; Kalantar-Zadeh, K.; Kis, A.; Coleman, J. N.; Strano, M. S. Electronics and Optoelectronics of Two-Dimensional Transition Metal Dichalcogenides. *Nat. Nanotechnol.* **2012**, *7*, 699–712.
4. Chhowalla, M.; Shin, H. S.; Ead, G.; Li, L.-J.; Loh, K. P.; Zhang, H. The Chemistry of Two-Dimensional Layered Transition Metal Dichalcogenide Nanosheets. *Nat. Chem.* **2013**, *5*, 263–275.
5. Huang, X.; Zeng, Z.; Zhang, H. Metal Dichalcogenide Nanosheets: Preparation, Properties and Applications. *Chem. Soc. Rev.* **2013**, *42*, 1934–1946.
6. Splendiani, A.; Sun, L.; Zhang, Y.; Li, T.; Kim, J.; Chim, C.-Y.; Galli, G.; Wang, F. Emerging Photoluminescence in Monolayer MoS_2. *Nano Lett.* **2010**, *10*, 1271–1275.
7. Geim, A. K.; Grigorieva, I. van der Waals Heterostructures. *Nature* **2013**, *499*, 419–425.
8. Britnell, L.; Ribeiro, R.; Eckmann, A.; Jalil, R.; Belle, B.; Mishchenko, A.; Kim, Y.-J.; Gorbachev, R.; Georgiou, T.; Morozov, S.; et al. Strong Light−Matter Interactions in Heterostructures of Atomically Thin Films. *Science* **2013**, *340*, 1311–1314.
9. Mak, K. F.; Lee, C.; Hone, J.; Shan, J.; Heinz, T. F. Atomically Thin MoS_2: A New Direct-Gap Semiconductor. *Phys. Rev. Lett.* **2010**, *105*, 136805.
10. Mak, K. F.; McGill, K. L.; Park, J.; McEuen, P. L. The Valley Hall Effect in MoS_2 Transistors. *Science* **2014**, *27*, 1489–1492.
11. Cao, T.; Wang, G.; Han, W.; Ye, H.; Zhu, C.; Shi, J.; Niu, Q.; Tan, P.; Wang, E.; Liu, B.; et al. Valley-Selective Circular Dichroism of Monolayer Molybdenum Disulphide. *Nat. Commun.* **2012**, *3*, 887.
12. Mak, K. F.; He, K.; Shan, J.; Heinz, T. F. Control of Valley Polarization in Monolayer MoS_2 by Optical Helicity. *Nat. Nanotechnol.* **2012**, *7*, 494–498.
13. Bernardi, M.; Palummo, M.; Grossman, J. C. Extraordinary Sunlight Absorption and One Nanometer Thick Photovoltaics Using Two-Dimensional Monolayer Materials. *Nano Lett.* **2013**, *13*, 3664–3670.
14. Feng, J.; Qian, X.; Huang, C.-W.; Li, J. Strain-Engineered Artificial Atom as a Broad-Spectrum Solar Energy Funnel. *Nat. Photonics* **2012**, *6*, 866–872.
15. Jaramillo, T. F.; Jørgensen, K. P.; Bonde, J.; Nielsen, J.H.; Horch, S.; Chorkendorff, I. Identification of Active Edge Sites for Electrochemical H_2 Evolution from MoS_2 Nanocatalysts. *Science* **2007**, *317*, 100–102.
16. Huang, X.; Zeng, Z.; Bao, S.; Wang, M.; Qi, X.; Fan, Z.; Zhang, H. Solution-Phase Epitaxial Growth of Noble Metal Nanostructures on Dispersible Single-Layer Molybdenum Disulfide Nanosheets. *Nat. Commun.* **2013**, *4*, 1444.
17. Shi, J.; Ma, D.; Han, G.-F.; Zhang, Y.; Ji, Q.; Gao, T.; Sun, J.; Song, X.; Li, C.; Zhang, Y.; et al. Controllable Growth and Transfer of Monolayer MoS_2 on Au Foils and Its Potential Application in Hydrogen Evolution Reaction. *ACS Nano* **2014**, *8*, 10196–10204.
18. Lee, C.; Yan, H.; Brus, L. E.; Heinz, T. F.; Hone, J.; Ryu, S. Anomalous Lattice Vibrations of Single- and Few-Layer MoS_2. *ACS Nano* **2010**, *4*, 2695–2700.
19. Shi, Y.; Zhou, W.; Lu, A.-Y.; Fang, W.; Lee, Y.-H.; Hsu, A. L.; Kim, S. M.; Kim, K. K.; Yang, H. Y.; Li, L.-J.; et al. van der Waals Epitaxy of MoS_2 Layers Using Graphene as Growth Templates. *Nano Lett.* **2012**, *12*, 2784–2791.
20. Wang, X.; Feng, H.; Wu, Y.; Jiao, L. Controlled Synthesis of Highly Crystalline MoS_2 Flakes by Chemical Vapor Deposition. *J. Am. Chem. Soc.* **2013**, *135*, 5304–5307.
21. Lee, Y.-H.; Zhang, X.-Q.; Zhang, W.; Chang, M.-T.; Lin, C.-T.; Chang, K.-D.; Yu, Y.-C.; Wang, J. T.-W.; Chang, C.-S.; Li, L.-J.; et al. Synthesis of Large-Area MoS_2 Atomic Layers with Chemical Vapor Deposition. *Adv. Mater.* **2012**, *24*, 2320–2325.
22. Lee, Y.-H.; Yu, L.; Wang, H.; Fang, W.; Ling, X.; Shi, Y.; Lin, C.-T.; Huang, J.-K.; Chang, M.-T.; Chang, C.-S.; et al. Synthesis and Transfer of Single-Layer Transition Metal Disulfides on Diverse Surfaces. *Nano Lett.* **2013**, *13*, 1852–1857.
23. Zhang, W.; Huang, J.-K.; Chen, C.-H.; Chang, Y.-H.; Cheng, Y.-J.; Li, L.-J. High-Gain Phototransistors Based on a CVD MoS_2 Monolayer. *Adv. Mater.* **2013**, *25*, 3456–3461.
24. Ling, X.; Lee, Y.-H.; Lin, Y.; Fang, W.; Yu, L.; Dresselhaus, M. S.; Kong, J. Role of the Seeding Promoter in MoS_2 Growth by Chemical Vapor Deposition. *Nano Lett.* **2014**, *14*, 464–472.
25. Najmaei, S.; Liu, Z.; Zhou, W.; Zou, X.; Shi, G.; Lei, S.; Yakobson, B. I.; Idrobo, J.-C.; Ajayan, P. M.; Lou, L. Vapour Phase Growth and Grain Boundary Structure of Molybdenum Disulphide Atomic Layers. *Nat. Mater.* **2013**, *12*, 754–759.
26. Hong, X.; Kim, J.; Shi, S.-F.; Zhang, Y.; Jin, C.; Sun, Y.; Tongay, S.; Wu, J.; Zhang, Y.; Wang, F. Ultrafast Charge Transfer in Atomically Thin MoS_2/WS_2 Heterostructures. *Nat. Nanotechnol.* **2014**, *9*, 682–686.
27. van der Zande, A. M.; Huang, P. Y.; Chenet, D. A.; Berkelbach, T. C.; You, Y.; Lee, G.-H.; Heinz, T. F.; Reichman, D. R.; Muller, D. A.; Hone, J. C. Grains and Grain Boundaries in Highly Crystalline Monolayer Molybdenum Disulphide. *Nat. Mater.* **2013**, *12*, 554–561.

28. Ji, Q.; Zhang, Y.; Gao, T.; Zhang, Y.; Ma, D.; Liu, M.; Chen, Y.; Qiao, X.; Tan, P.-H.; Kan, M.; et al. Epitaxial Monolayer MoS_2 on Mica with Novel Photoluminescence. *Nano Lett.* **2013**, *13*, 3870–3877.
29. Zhang, Y.; Zhang, Y.; Ji, Q.; Ju, J.; Yuan, H.; Shi, J.; Gao, T.; Ma, D.; Liu, M.; Chen, Y.; et al. Controlled Growth of High-Quality Monolayer WS_2 Layers on Sapphire and Imaging Its Grain Boundary. *ACS Nano* **2013**, *7*, 8963–8971.
30. Zhang, Y.; Ji, Q.; Han, G.-F.; Ju, J.; Shi, J.; Ma, D.; Sun, J.; Zhang, Y.; Li, M.; Lang, X.-Y.; et al. Dendritic, Transferable, Strictly Monolayer MoS_2 Flakes Synthesized on $SrTiO_3$ Single Crystals for Efficient Electrocatalytic Applications. *ACS Nano* **2014**, *8*, 8617–8624.
31. Sørensen, S. G.; Füchtbauer, H. G.; Tuxen, A. K.; Walton, A. S.; Lauritsen, J. V. Structure and Electronic Properties of *In Situ* Synthesized Single-Layer MoS_2 on a Gold Surface. *ACS Nano* **2014**, *8*, 6788–6796.
32. Wood, J. D.; Schmucker, S. W.; Lyons, A. S.; Pop, E.; Lyding, J. W. Effects of Polycrystalline Cu Substrate on Graphene Growth by Chemical Vapor Deposition. *Nano Lett.* **2011**, *11*, 4547–4554.
33. Murdock, A. T.; Koos, A.; Britton, T. B.; Houben, L.; Batten, T.; Zhang, T.; Wilkinson, A. J.; Dunin-Borkowski, R. E.; Lekka, C. E.; Grobert, N. Controlling the Orientation, Edge Geometry, and Thickness of Chemical Vapor Deposition Graphene. *ACS Nano* **2013**, *7*, 1351–1359.
34. Hayashi, K.; Sato, S.; Ikeda, M.; Kaneta, C.; Yokoyama, N. Selective Graphene Formation on Copper Twin Crystals. *J. Am. Chem. Soc.* **2012**, *134*, 12492–12498.
35. Terrones, H.; Del Corro, E.; Feng, S.; Poumirol, J.; Rhodes, D.; Smirnov, D.; Pradhan, N.; Lin, Z.; Nguyen, M.; Elias, A.; et al. New First Order Raman-Active Modes in Few Layered Transition Metal Dichalcogenides. *Sci. Rep.* **2014**, *4*, 4215.
36. Zhao, Y.; Luo, X.; Li, H.; Zhang, J.; Araujo, P. T.; Gan, C. K.; Wu, J.; Zhang, H.; Quek, S. Y.; Dresselhaus, M. S.; et al. Interlayer Breathing and Shear Modes in Few-Trilayer MoS_2 and WSe_2. *Nano Lett.* **2013**, *13*, 1007–1015.
37. Huang, K.; Gibbs, D.; Zehner, D.; Sandy, A.; Mochrie, S. Phase Behavior of the Au(111) Surface: Discommensurations and Kinks. *Phys. Rev. Lett.* **1990**, *65*, 3313–3316.
38. Chambliss, D.; Wilson, R.; Chiang, S. Nucleation of Ordered Ni Island Arrays on Au(111) by Surface-Lattice Dislocations. *Phys. Rev. Lett.* **1991**, *66*, 1721–1724.
39. Meyer, J.; Baikie, I.; Kopatzki, E.; Behm, R. J. Preferential Island Nucleation at the Elbows of the Au(111) Herringbone Reconstruction through Place Exchange. *Surf. Sci.* **1996**, *365*, L647–L651.
40. Park, J.; Lee, J.; Liu, L.; Clark, K.; Durand, C.; Park, C.; Sumpter, B.; Baddorf, A.; Mohsin, A.; Yoon, M.; et al. Spatially Resolved One-Dimensional Boundary States in Graphene-Hexagonal Boron Nitride Planar Heterostructures. *Nat. Commun.* **2014**, *5*, 5403.
41. Lee, J.-H.; Lee, E. K.; Joo, W.-J.; Jang, Y.; Kim, B.-S.; Lim, J. Y.; Choi, S.-H.; Ahn, S. H.; Ahn, J. R.; Park, M.-H.; et al. Wafer-Scale Growth of Single-Crystal Monolayer Graphene on Reusable Hydrogen-Terminated Germanium. *Science* **2014**, *344*, 286–289.
42. Kresse, G.; Furthmüller, J. Efficient Iterative Schemes for *Ab Initio* Total-Energy Calculations Using a Plane-Wave Basis Set. *Phys. Rev. B* **1996**, *54*, 11169–11186.
43. Blöchl, P. E. Projector Augmented-Wave Method. *Phys. Rev. B* **1994**, *50*, 17953–17979.
44. Kresse, G.; Joubert, D. From Ultrasoft Pseudopotentials to the Projector Augmented-Wave Method. *Phys. Rev. B* **1999**, *59*, 1758–1775.
45. Perdew, J. P.; Burke, K.; Ernzerhof, M. Generalized Gradient Approximation Made Simple. *Phys. Rev. Lett.* **1996**, *77*, 3865–3868.
46. Bengió, S.; Navarro, V.; González-Barrio, M.; Cortés, R.; Vobornik, I.; Michel, E. G.; Mascaraque, A. Electronic Structure of Reconstructed Au(100): Two-Dimensional and One-Dimensional Surface States. *Phys. Rev. B* **2012**, *86*, 045426.
47. Methfessel, M.; Paxton, A. High-Precision Sampling for Brillouin-Zone Integration in Metals. *Phys. Rev. B* **1989**, *40*, 3616–3621.
48. Grimme, S.; Antony, J.; Ehrlich, S.; Krieg, H. A Consistent and Accurate *Ab Initio* Parametrization of Density Functional Dispersion Correction (DFT-D) for the 94 Elements H-Pu. *J. Chem. Phys.* **2010**, *132*, 154104.
49. Grimme, S.; Ehrlich, S.; Goerigk, L. Effect of the Damping Function in Dispersion Corrected Density Functional Theory. *J. Comput. Chem.* **2011**, *32*, 1456–1465.